Physics-Informed Neural Networks for MIMO Beam Map and Environment Reconstruction

Wangqian Chen, Junting Chen and Shuguang Cui

Abstract—As communication networks evolve towards greater complexity (e.g., 6G and beyond), a deep understanding of the wireless environment becomes increasingly crucial. When explicit knowledge of the environment is unavailable, geometry-aware feature extraction from channel state information (CSI) emerges as a pivotal methodology to bridge physical-layer measurements with network intelligence. This paper proposes to explore the received signal strength (RSS) data, without explicit 3D environment knowledge, to jointly construct the radio beam map and environmental geometry for a multiple-input multiple-output (MIMO) system. Unlike existing methods that only learn blockage structures, we propose an oriented virtual obstacle model that captures the geometric features of both blockage and reflection. Reflective zones are formulated to identify relevant reflected paths according to the geometry relation of the environment. We derive an analytical expression for the reflective zone and further analyze its geometric characteristics to develop a reformulation that is more compatible with deep learning representations. A physics-informed deep learning framework that incorporates the reflective-zone-based geometry model is proposed to learn the blockage, reflection, and scattering components, along with the beam pattern, which leverages physics prior knowledge to enhance network transferability. Numerical experiments demonstrate that, in addition to reconstructing the blockage and reflection geometry, the proposed model can construct a more accurate MIMO beam map with a 32%−48% accuracy improvement.

Index Terms—MIMO radio map, channel modeling, beamforming, reflection characterization, deep learning

I. INTRODUCTION

MASSIVE MIMO transmission techniques have enabled efficient spatial multiplexing, significant beamforming gain, and flexible interference mitigation, which have found success in 5G networks and beyond. However, to achieve the full benefit of MIMO systems, the high dimensional CSI is needed, which imposes significant channel training overhead. In this context, MIMO beam maps are constructed as charts or structured representations that capture the spatial characteristics of the MIMO channel. Specifically, MIMO beam maps may enable interference management and adaptive beamforming without exhaustive channel training [1]–[3], and they have been exploited for optimizing beam alignment and signal power allocation for energy efficiency enhancement [4]. However, while there have been some investigations on the exploitation of MIMO beam maps, little is known in the literature on the efficient construction of MIMO beam maps.

The fundamental challenge of MIMO beam map construction is the demand of a large volume of measurement data. While there have been some works on power spectrum map or radio environment map construction using statistical methods [5, 6], interpolation [7, 8], tensor completion [9, 10] and deep learning approaches [11]–[13], these works mainly focused on constructing the RSS at each location without considering the beam pattern of the antenna array. However, constructing a MIMO beam map can be much more challenging than constructing a power spectrum map. First, a MIMO beam map is expected to capture higher dimensional CSI at each location as opposed to conventional power maps that only capture the aggregate power. Second, a MIMO beam map tends to experience larger spatial variations, because the signal strength is affected *not only* by the propagation environment, but also by the MIMO beam pattern. Thus, following a conventional interpolation or tensor completion type approach, more measurements will be needed. Third, the MIMO beam map is more sensitive to the propagation environment, as it captures received power across beam directions, which is much less homogeneous as compared to conventional power maps.

Ray tracing (RT) methods have been adopted to construct MIMO beam maps by simulating reflection, diffraction, and scattering [14, 15]. While RT provides detailed spatial and temporal information about CSI, the cost of the detailed environmental geometry, the computational complexity and the memory requirements are prohibitively large. To accelerate computation, several studies leveraged the power of neural networks to infer implicit CSI mappings directly from raw RT data [16, 17]. More end-to-end neural network architectures, such as generative adversarial networks [18] or deep autoencoders [19], were proposed for CSI learning. However, these methods still relied heavily on detailed environmental information, such as precise city maps, which limits their applicability in scenarios where the environmental information is incomplete or unavailable. Channel charting was also employed to learn low-dimensional charts of CSI while pre-

serving the local geometry of the channel [20]–[22]. However, recovering location labels for radio map construction remains a non-trivial challenge due to the inherent complexity and ambiguity in mapping CSI to physical coordinates.

To summarize, the existing deep learning approaches for MIMO beam map construction lack a clear *physics model* and rely purely on data, without explicitly exploiting the geometric relationship between channel measurements and the environment. Consequently, it is not clear whether the learned knowledge can be transferred to new scenarios. Although it is possible to extend a power map to a MIMO beam map with the MIMO steering vectors in line-of-sight (LOS) scenarios, predicting the directionality of beamforming gains in non-line-of-sight (NLOS) conditions is challenging due to blockages and reflections. While classical methods can construct MIMO beam maps independently for each individual beam pattern, they may fail to capture inherent correlation among beams, and thus the required amount of training data scales linearly over the number of antennas, which is highly inefficient.

This paper attempts to build a deep learning model for MIMO beam map construction embedded with explicit propagation model and environment model. We propose to reconstruct the environmental geometry as an intermediate step to assist for the MIMO beam map construction, since all the beams of all transmitters (TXs) share the same propagation environment. Such a process resembles radio tomography [23], which solves an inverse problem of reconstructing the environment from RSS measurements. While our earlier attempts [24, 25] proposed virtual obstacles to capture the environmental geometry, they are limited to reconstructing the blockage features, while reconstructing the reflection characteristics remains a challenge. Furthermore, instead of pursuing accuracy in environment reconstruction, our goal is to learn a geometric representation of the environment shared among TXs for the best inference of the MIMO beam map.

Specifically, we address the challenges by leveraging blockage and reflection geometry in neural network design to jointly construct the MIMO beam map and virtual environment using only RSS measurements. Towards this end, we propose to learn a set of *oriented virtual obstacles* at possible locations, where each oriented virtual obstacle consists of two attributes: height that determines whether a signal can be blocked or reflected, and orientation that determines the direction of signal reflection. By exploiting the geometric relationship between paths and oriented virtual obstacles, a physics-informed model that incorporates the beam pattern is proposed to capture the channel attenuation of the direct path and reflected paths. To tackle the challenge of solving an *inverse RT problem* that reconstructs oriented virtual obstacles from RSS measurements, we address this complex inverse problem by introducing the notion of *reflective zones* to identify a subset of relevant propagation paths based on environmental geometry. In addition, a model embedded neural network is developed to incorporate the *reflective-zone-based geometry model* for a joint MIMO beam map and oriented virtual obstacle construction. Our implementation and experiments show that such a physics-informed design simplifies the modeling complexity of the neural network, and shows a great transferability to generate
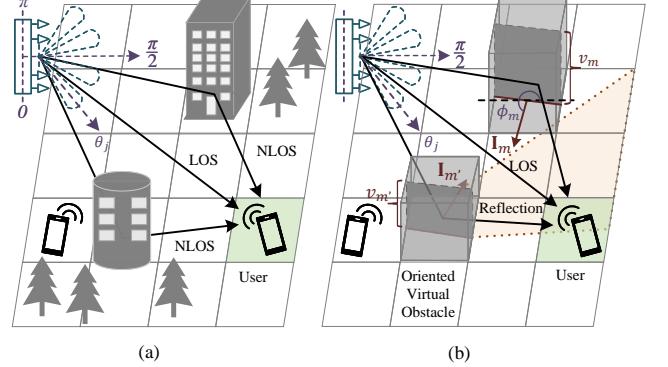

Figure 1. a) A multipath propagation scenario with direct and single-bounce reflection paths; b) Oriented virtual obstacles that describe the geometry of the environment.

new MIMO beam maps in previously unseen scenarios.

The novelty and contribution are summarized as follows:

- We propose a physics-informed neural network architecture to *jointly* construct the MIMO beam map and 3D environment from RSS measurements. As the model explicitly learns the MIMO beam model, the environment, and how the signal interacts with the environment, it may reconstruct the MIMO beam maps much more efficiently.
- We introduce the concept of reflective zones as deep learning representation for signal reflection, and based on the geometry relation, we derive simplified conditions that can be easily implemented in a deep learning framework to characterize signal reflection.
- Numerical experiments demonstrate that the proposed model achieves over 30% improvement in MIMO beam map accuracy compared to existing deep learning based approaches, and exhibits superior extrapolation capabilities to previously unseen scenarios.

In addition, we present an application of beam alignment where the proposed method can reduce the search overhead by 78% compared to exhaustive beam sweeping.

The rest of the paper is organized as follows. Section II reviews the system model, while Section III analyzes the reflective zone. Section IV discusses the proposed learning framework. Design examples are presented in Section V and conclusions are drawn in Section VI.

Notations: $(\cdot)^{\mathrm{T}}$ and $(\cdot)^*$ represent the transpose and Hermitian transpose operations, respectively. $|\cdot|$ denotes the absolute value and $\|\cdot\|$ represents the L_2 norm. $\overrightarrow{\mathbf{xy}}$ denotes the vector from position $\mathbf{x}$ to position $\mathbf{y}$, while $\mathbf{x} \cdot \mathbf{y}$ represents the dot product of vectors $\mathbf{x}$ and $\mathbf{y}$, and therefore, $\mathbf{x} \cdot \mathbf{y} = \mathbf{x}^{\mathrm{T}}\mathbf{y}$.

II. System Model

Consider a massive MIMO communication system with multiple base stations (BSs) in an outdoor urban environment. The BSs, treated as TXs, equip with multiple antennas, and all ground nodes, treated as receivers (RXs), are single-antenna devices. For multi-antenna RXs, they can be considered as multiple co-located virtual single-antenna RXs. Denote a wireless link $\tilde{\mathbf{p}} = (\mathbf{p}_{\mathrm{t}}, \mathbf{p}_{\mathrm{r}}) \in \mathbb{R}^6$ using the position pair $\mathbf{p}_{\mathrm{t}}, \mathbf{p}_{\mathrm{r}} \in \mathbb{R}^3$ of the TX and the RX, respectively.

The narrow-band channel of $\tilde{\mathbf{p}}$ can be expressed as

$$\mathbf{h}(\tilde{\mathbf{p}}) = \sum_{l=0}^{L} \beta_l \mathbf{a}^*(\phi_l(\tilde{\mathbf{p}})) \qquad (1)$$

where $\beta_l \sim \mathcal{CN}(0, \sigma_l^2)$ is the complex gain of the lth propagation path with zero mean and variance σ_l^2, which captures the path loss, and $\mathbf{a}(\phi_l)$ denotes the array response vector for angle of departure (AOD) ϕ_l. For example, in case of a uniform linear antenna array (ULA), the array response vector can be formulated as

$$\mathbf{a}(\phi_l) = \frac{1}{\sqrt{N_t}}[1, e^{-i2\pi\frac{\Delta}{\lambda}\cos\phi_l}, ..., e^{-i2\pi\frac{\Delta}{\lambda}(N_t-1)\cos\phi_l}]^{\mathrm{T}} \qquad (2)$$

where $i = \sqrt{-1}$ is the imaginary unit, λ is the carrier wavelength, and Δ stands for the antenna spacing.

A codebook-based approach at the BS is applied to construct MIMO beams for channel measurement. Denote $\mathbf{w}_j$ as the jth beamforming vector from a codebook $\mathcal{W}$ that satisfies the power constrain with $|\mathbf{w}_j^*\mathbf{w}_j| = 1$. The beam pattern over a range of angle ϕ of the jth beam is given by

$$B(\phi, \mathbf{w}_j) = |\mathbf{a}^*(\phi)\mathbf{w}_j|^2. \qquad (3)$$

It is assumed that the beamforming vectors $\mathbf{w}_j$ are designed according to the antenna array geometry such that the beam pattern $B(\phi, \mathbf{w}_j)$ concentrates the energy in one specific main-lobe direction θ_j and the beamforming gain decreases as the angle deviates from the direction θ_j as shown in Fig. 2(a). It is also assumed that the number of antennas N_t at the BS is large, such that the sidelobe energy is negligible compared to the measurement noise. Moreover, the collection $\mathcal{W}$ of the beamforming vectors $\mathbf{w}_j$ are carefully designed such that these beams cover the entire angular space as illustrated in Fig. 2(b).

An example under ULA is to adopt the discrete Fourier transform (DFT) codebook. It is known that in the LOS case under a large N_t, the DFT matrix approximately diagonalizes the channel covariance matrix, and hence, using DFT beams may obtain a good characterization of the MIMO channel.

The measurement for the channel of $\tilde{\mathbf{p}}$ using beamforming vector $\mathbf{w}_j$ is given by

$$\rho(\tilde{\mathbf{p}}, \mathbf{w}_j) = \mathbb{E}\left[|\mathbf{h}(\tilde{\mathbf{p}})\mathbf{w}_j|^2\right] + n \qquad (4)$$

where $\mathbb{E}[\cdot]$ denotes the expectation over the randomness from the small-scale fading, and n denotes the measurement noise and the uncertainty due to the small-scale fading.

For each location pair $\tilde{\mathbf{p}}$, a set of measurements $\rho(\tilde{\mathbf{p}}, \mathbf{w}_j)$ are taken for $j = 1, 2, \ldots, |\mathcal{W}|$, where $|\mathcal{W}|$ denotes the number of beamforming vectors in the codebook $\mathcal{W}$. The goal of the paper is to build a model to generate MIMO beam maps $g(\tilde{\mathbf{p}}, \mathbf{w}_j)$ for all possible location pairs $\tilde{\mathbf{p}}$ over all beams $\mathbf{w}_j \in \mathcal{W}$ from a set of limited measurements $\{\rho(\tilde{\mathbf{p}}, \mathbf{w}_j), \tilde{\mathbf{p}}\}$.

A. Environment-Embedded Radio Map Model

We adopt an oriented virtual obstacle model to describe the propagation environment as follows. Partition the ground area of interest into M grid cells and denote D as the grid spacing. The oriented virtual obstacle on the mth grid cell is modeled
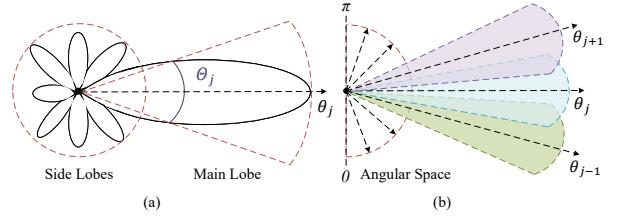

Figure 2. a) The beam pattern studied consists of a main lobe and several sidelobes; b) The beams are designed to collectively cover the angular space.

as an oriented cube of a certain height perpendicular to the ground, and the cube may block the signal or reflect it to a specific direction based on its orientation, as shown in Fig. 1.

Specifically, denote v_m as the height of the virtual obstacle and $\phi_m \in [0, 2\pi)$ as the normal angle of its orientation on the mth grid cell, respectively. The normal angle ϕ_m can also be captured by its normal vector $\mathbf{l}_m$, where $\mathbf{l}_m = (\cos\phi_m, \sin\phi_m, \eta)$ and η is a constant. Denote $\mathbf{V}_{\mathrm{H}}$ as the matrix form of v_m such that the (x, y)th entry of $\mathbf{V}_{\mathrm{H}}$ denotes the height at the (x, y)th grid cell. Similar notation $\mathbf{V}_\Phi$ is defined for the normal angle ϕ_m. The environmental geometry is fully captured by the concatenated variable $\mathbf{V} = [\mathbf{V}_{\mathrm{H}}, \mathbf{V}_\Phi]$.

Denote $\varphi(\boldsymbol{x}, \boldsymbol{y})$ as the direction angle of location $\boldsymbol{x}$ relative to location $\boldsymbol{y}$, and $\mathbf{c}_m$ as the coordinates of the mth grid cell. We formulate the first term in the measurement model (4) using an environment-embedded radio map model as

$$\begin{aligned} g(\tilde{\mathbf{p}}, \mathbf{w}_j; \mathbf{V}) = & B(\varphi(\mathbf{p}_{\mathrm{t}}, \mathbf{p}_{\mathrm{r}}), \mathbf{w}_j)g_0(\tilde{\mathbf{p}}, \mathbf{V}) \\ & + \sum_m B(\varphi(\mathbf{p}_{\mathrm{t}}, \mathbf{c}_m), \mathbf{w}_j)g_{\mathrm{r}}^m(\tilde{\mathbf{p}}, \mathbf{w}_j, \mathbf{V}) \\ & + g_{\mathrm{s}}(\tilde{\mathbf{p}}, \mathbf{w}_j, \mathbf{V}) \end{aligned} \qquad (5)$$

where the three terms characterize the following phenomenon:

- Direct path: In the first term, the function $B(\varphi(\mathbf{p}_{\mathrm{t}}, \mathbf{p}_{\mathrm{r}}), \cdot)$ captures the beam pattern for the direct path from $\mathbf{p}_{\mathrm{t}}$ to $\mathbf{p}_{\mathrm{r}}$, and the function $g_0(\cdot)$ models the path gain of the direct path based on the geometry of the environment $\mathbf{V}$.
- Reflected paths: All virtual obstacles have the potential to reflect the signals from the TX, and some of them reach the RX. Thus, the second term of (5) aggregates contributions from all possible reflected paths. The function $B(\varphi(\mathbf{p}_{\mathrm{t}}, \mathbf{c}_m), \cdot)$ captures the beam pattern of the reflected path bounced by the mth virtual obstacle, and the function $g_{\mathrm{r}}^m(\cdot)$ models the reflected path gain.
- Scattering paths: The third term $g_{\mathrm{s}}(\cdot)$ accounts for the residual fluctuation due to scattering.

We further focus on designing simple representations for each component to enable efficient learning of the model (5).

B. Blockage Model

We establish a simplified representation for the relationship between the direct path gain $g_0(\tilde{\mathbf{p}}, \mathbf{V})$ and the environment $\mathbf{V}$.

Denote $\mathcal{B}(\tilde{\mathbf{p}})$ as the set of grid cells covered by the line segment joining $\mathbf{p}_{\mathrm{t}}$ and $\mathbf{p}_{\mathrm{r}}$. For each grid cell $m \in \mathcal{B}(\tilde{\mathbf{p}})$, denote $z_m(\tilde{\mathbf{p}})$ as the height of the line segment of $\tilde{\mathbf{p}}$ that passes over the mth grid cell. Denote $\tilde{\mathcal{D}}_0$ as the set of links $\tilde{\mathbf{p}}$ which are not blocked by any virtual obstacle, and $\tilde{\mathcal{D}}_0$ is

termed as the LOS region in this paper. Similarly, $\tilde{\mathcal{D}}_1$ denotes the NLOS region.

Mathematically, for an LOS case $\tilde{\mathbf{p}} \in \tilde{\mathcal{D}}_0$, we have $v_m < z_m(\tilde{\mathbf{p}})$ for all grid cells $m \in \mathcal{B}(\tilde{\mathbf{p}})$, where recall that v_m is the height of the virtual obstacle at the mth grid cell; for a NLOS case $\tilde{\mathbf{p}} \in \tilde{\mathcal{D}}_1$, we have $v_m \geq z_m(\tilde{\mathbf{p}})$ for at least one grid cell $m \in \mathcal{B}(\tilde{\mathbf{p}})$, *i.e.*, the direct path from $\mathbf{p}_t$ to $\mathbf{p}_r$ is blocked by at least one of the virtual obstacles along the direct path. Thus, a model for the LOS region $\tilde{\mathcal{D}}_0(\mathbf{V}_H)$ given the parameter $\mathbf{V}_H$ for the heights of the virtual obstacles can be formulated as

$$\mathbb{I}\{\tilde{\mathbf{p}} \in \tilde{\mathcal{D}}_0(\mathbf{V}_H)\} = \prod_{m \in \mathcal{B}(\tilde{\mathbf{p}})} \mathbb{I}\{v_m < z_m(\tilde{\mathbf{p}})\} \qquad (6)$$

and the model for the NLOS region can also be obtained by $\mathbb{I}\{\tilde{\mathbf{p}} \in \tilde{\mathcal{D}}_1(\mathbf{V}_H)\} = 1 - \mathbb{I}\{\tilde{\mathbf{p}} \in \tilde{\mathcal{D}}_0(\mathbf{V}_H)\}$, where $\mathbb{I}\{A\}$ is an indicator function that takes value 1 if condition A is true, and 0, otherwise. As a result, the blockage-aware channel gain of the direct path of $\tilde{\mathbf{p}}$ is modeled as

$$g_0(\tilde{\mathbf{p}}, \mathbf{V}_H) = \sum_{k=\{0,1\}} f_k(d(\mathbf{p}_t, \mathbf{p}_r))\mathbb{I}\{\tilde{\mathbf{p}} \in \tilde{\mathcal{D}}_k(\mathbf{V}_H)\} \qquad (7)$$

where $f_k(\cdot)$ are the path gain functions for the LOS and NLOS channels, respectively, and $d(\mathbf{p}_t, \mathbf{p}_r) = \|\mathbf{p}_t - \mathbf{p}_r\|$ represents the distance between the TX at $\mathbf{p}_t$ and the RX at $\mathbf{p}_r$.

C. Reflection Model

We exploit the following two properties to construct a lightweight reflection model with reduced parameters.

First, it practically suffices to consider the reflection from the main lobe of the beam. Because from the beam pattern model (3) as illustrated in Fig. 2, there is only one main lobe, and in a typical massive MIMO scenario, the side lobes have substantially lower power than that of the main lobe, which is already very small due to reflection. Thus, for a link $\tilde{\mathbf{p}}$, the energy from the reflection of side lobes can be ignored.

Second, in many scenarios, the paths with a single reflection dominate the energy over paths with multiple reflections.[1] This is because paths with multiple reflections tend to travel over a longer distance and each reflection loses energy.

Therefore, we propose to consider only the paths with a single reflection and aligned with the main lobe.

1) Main Lobe Area: The main lobe area $\tilde{\mathcal{M}}(\mathbf{p}_t, \mathbf{w}_j)$ is defined as the set of grid cells within the main lobe coverage of the jth beam from the TX at $\mathbf{p}_t$. From the beam pattern model (3), the main lobe for the jth beamforming vector $\mathbf{w}_j$ is defined according to the beam angle θ_j and the beamwidth Θ_j as Fig. 2(a).[2] Thus, the main lobe area is formulated as

$$\mathbb{I}\{m \in \tilde{\mathcal{M}}(\mathbf{p}_t, \mathbf{w}_j)) = \mathbb{I}\{|\varphi(\mathbf{p}_t, \mathbf{c}_m) - \theta_j| \leq \Theta_j/2\}. \qquad (8)$$

---

[1]Exception scenarios may include tunnels that experience a canyon effect which acts like a waveguide that boosts the signals via multiple reflections. However, such scenarios occur infrequently and are not the focus of this paper.

[2]In our implementation, we use 3 dB beamwidth Θ_j, which refers to the angular range where the radiated power is within 3 dB of the maximum power.

2) Reflective Zone: The reflective zone $\tilde{\mathcal{Q}}_m(\mathbf{p}_t, \mathbf{V})$ of the virtual obstacle at the mth grid cell for the TX at $\mathbf{p}_t$ is defined as the region of RX locations $\mathbf{p}_r$ such that the signal emitted from the TX location $\mathbf{p}_t$ can be received at RX location $\mathbf{p}_r$ via a single specular reflection at the mth virtual obstacle as shown in Fig. 3(a). It is clear that the reflective zone depends on the orientation of the virtual obstacle captured by its normal vector $\mathbf{l}_m$, which is a model parameter to be learned.

Combining the notion of main lobe area and reflective zone, the reflection via the mth virtual obstacle is modeled as

$$\begin{aligned} g_r^m(\tilde{\mathbf{p}}, \mathbf{w}_j, \mathbf{V}) = \mathbb{I}\{m \in \tilde{\mathcal{M}}(\mathbf{p}_t, \mathbf{w}_j)\}\mathbb{I}\{\mathbf{p}_r \in \tilde{\mathcal{Q}}_m(\mathbf{p}_t, \mathbf{V})\} \\ \times f_r(d'(\tilde{\mathbf{p}}, \mathbf{c}_m), \mathbf{V}) \end{aligned}$$

$$(9)$$

where $d'(\tilde{\mathbf{p}}, \mathbf{c}_m) = d(\mathbf{p}_t, \mathbf{c}_m) + d(\mathbf{p}_r, \mathbf{c}_m)$ represents the propagation distance of the reflected path. The first condition $\mathbb{I}\{m \in \tilde{\mathcal{M}}(\mathbf{p}_t, \mathbf{w}_j)\}$ restricts the reflected location to the main lobe, the second condition $\mathbb{I}\{\mathbf{p}_r \in \tilde{\mathcal{Q}}_m(\mathbf{p}_t, \mathbf{V})\}$ models the reflective zone, and the final term $f_r(\cdot)$ captures the path gain when both conditions are satisfied.

The remaining challenge is to design a model for the reflective zone $\tilde{\mathcal{Q}}_m(\mathbf{p}_t, \mathbf{V})$. A more explicit mechanism shall be constructed for $\tilde{\mathcal{Q}}_m(\mathbf{p}_t, \mathbf{V})$ such that it can be learned efficiently under a deep learning framework.

D. Scattering Model

While the energy from the direct path and prominent reflections is captured by the first two terms in (5), a small residual may remain due to multiple reflections, diffraction, and scattering. Explicitly modeling these fine-grained propagation phenomena is highly challenging. To this end, a generic physical principle is exploited, where the propagation mainly depends on the local environment surrounding the TX and RX, since similar local geometry can exhibit analogous propagation paths (in terms of direction and quantity). As such, we adopt a model to map the local environment to the residual scattering, and more specifically, we employ such a scattering model from [25] and extend it to the MIMO beam scenario.

Define $\mathcal{B}_s(\tilde{\mathbf{p}}, \mathbf{V})$ as the set of grid cells within a local area around $\mathbf{p}_t$ and $\mathbf{p}_r$, where the area is defined as an ellipse with these positions as foci under a given eccentricity ratio as illustrated in [25]. The scattering model is thus given as

$$g_s(\tilde{\mathbf{p}}, \mathbf{w}_j, \mathbf{V}) = f_s(\mathcal{B}_s(\tilde{\mathbf{p}}, \mathbf{V}), \mathbf{w}_j) \qquad (10)$$

where $f_s(\cdot)$ is a mapping that depends on the beam $\mathbf{w}_j$ and the local geometric features of $\mathbf{V}$. Furthermore, $f_s(\cdot)$ should be invariant to an absolute offset and rotation of the coordinate system, such as the rotation and translation of $\mathcal{B}_s(\tilde{\mathbf{p}}, \mathbf{V})$.

Note that the design of the scattering model in [25] cannot capture the characteristics of MIMO beams, and therefore, the remaining challenge is to incorporate beam directionality and the associated beam selectivity into the model.

III. GEOMETRIC FEATURES OF REFLECTIVE ZONE

In this section, we derive the expression for the reflective zone condition $\mathbb{I}\{\mathbf{p}_r \in \tilde{\mathcal{Q}}_m(\mathbf{p}_t, \mathbf{V})\}$. Subsequently, we analyze its geometric features and develop a simplified reformulation more compatible with deep learning representations.

A. Analytical Characterization for the Reflective Zone

We first derive an analytical expression for $\mathbb{I}\{\mathbf{p}_r \in \tilde{\mathcal{Q}}_m(\mathbf{p}_t, \mathbf{V})\}$ in (9) that determines whether a position $\mathbf{p}_r$ can receive a reflected signal emitted from TX position $\mathbf{p}_t$ via the mth virtual obstacle with a certain orientation.

Using the concept of virtual TX in specular reflection, consider to abstract the virtual obstacle as a rectangular board perpendicular to the ground with a certain height as shown in Fig. 3(a) in a horizontal view. The orientation of the board is specified by the normal vector $\mathbf{l}_m$. The reflection received at the RX is equivalent to a direct path from the virtual TX^m, the mirror of the TX with respect to the board, to the RX. As a result, the reflective zone can be understood as the shadow of the rectangular board being illuminated by the virtual TX^m.

Mathematically, denote $\mathbf{p}_t^m$ as the position of the virtual TX relative to the mth grid cell. The board can be modeled using a 3D plane function as $\mathbf{l}_m \cdot (\mathbf{o}_p - \mathbf{c}_m) = 0$, where $\mathbf{o}_p$ denotes the point on the board. Similarly, the virtual direct path is modeled using a 3D line function as $\mathbf{o}_l = \mathbf{p}_r + l(\mathbf{p}_t^m - \mathbf{p}_r)$, where $\mathbf{o}_l$ is the point of the line and l denotes its scale factor. The intersection $\mathbf{o}_m$ of the two functions is identified by

$$\mathbf{o}_m = \mathbf{p}_r + \frac{\mathbf{l}_m \cdot (\mathbf{c}_m - \mathbf{p}_r)}{\mathbf{l}_m \cdot (\mathbf{p}_t^m - \mathbf{p}_r)}(\mathbf{p}_t^m - \mathbf{p}_r). \quad (11)$$

To ensure that the intersection $\mathbf{o}_m$ falls within the mth grid cell, we have the orientation conditions $|o_{m,i} - c_{m,i}|_{i=\{1,2\}} \le D/2$ under $0 \le (\mathbf{l}_m \cdot (\mathbf{c}_m - \mathbf{p}_r))/(\mathbf{l}_m \cdot (\mathbf{p}_t^m - \mathbf{p}_r)) \le 1$, and the height condition $o_{m,3} \le v_m$, where $o_{m,i}$ and $c_{m,i}$ denote the ith element of $\mathbf{o}_m$ and $\mathbf{c}_m$, respectively. Therefore, the reflective zone condition in (9) can be formulated as

$$\mathbb{I}\{\mathbf{p}_r \in \tilde{\mathcal{Q}}_m(\mathbf{p}_t, \mathbf{V})\} = \prod_{i=\{1,2\}} \mathbb{I}\{|o_{m,i} - c_{m,i}| \le D/2\}$$
$$\times \mathbb{I}\{0 \le \frac{\mathbf{l}_m \cdot (\mathbf{c}_m - \mathbf{p}_r)}{\mathbf{l}_m \cdot (\mathbf{p}_t^m - \mathbf{p}_r)} \le 1\} \quad (12)$$
$$\times \mathbb{I}\{o_{m,3} \le v_m\}$$

Although an explicit expression is found in (12), solving an inverse problem to learn the geometric parameters v_m and $\mathbf{l}_m$ is still challenging. This is due to the nonlinear expression for $\mathbf{l}_m$ in (11) and the multiple indicator functions in (12), which easily lead to gradient vanishing or explosion in a deep neural network. To this end, we further simplify (12) by decomposing the terms for the height v_m and the orientation $\mathbf{l}_m$ as follows.

B. Height Condition for the Reflective Zone

We show that the term $\mathbb{I}\{o_{m,3} \le v_m\}$ in (12) which couples the parameters v_m and $\mathbf{l}_m$ via $\mathbf{o}_m$ in (11) can be simplified into an expression involving only the obstacle heigh v_m.

Denote $\mathbf{c}_m = (\bar{\mathbf{c}}_m, c_{m,3})$, where $\bar{\mathbf{c}}_m = (c_{m,1}, c_{m,2}) \in \mathbb{R}^2$ is the ground projected location. Similar notations $\mathbf{p}_t = (\bar{\mathbf{p}}_t, p_{t,3})$ and $\mathbf{p}_r = (\bar{\mathbf{p}}_r, p_{r,3})$ are defined for the TX and RX, respectively. By the law of reflection, the locations $\mathbf{p}_t^m$, $\mathbf{c}_m$ and $\mathbf{p}_r$ are collinear as shown in Fig. 3(c), where the virtual obstacle in vertical direction is simplified as a line segment
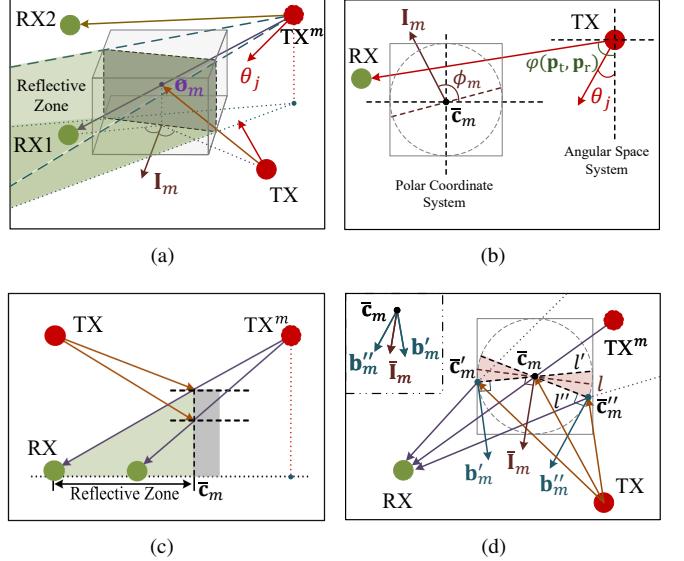

(a)

(b)

(c)

(d)

Figure 3. a) The diagram of the reflective zone geometry; b) The relationship between the polar coordinate system and the angular space; c) The geometry of the height condition for the reflective zone; d) The geometry of the orientation condition for the reflective zone.

that perpendicular to the ground. Denote $l_m = (\mathbf{l}_m \cdot (\mathbf{c}_m - \mathbf{p}_r))/(\mathbf{l}_m \cdot (\mathbf{p}_t^m - \mathbf{p}_r))$, we can reformulate it as

$$l_m = \|\mathbf{c}_m - \mathbf{p}_r\| / \|\mathbf{p}_t^m - \mathbf{p}_r\|$$
$$= d(\bar{\mathbf{c}}_m, \bar{\mathbf{p}}_r) / (d(\bar{\mathbf{c}}_m, \bar{\mathbf{p}}_r) + d(\bar{\mathbf{c}}_m, \bar{\mathbf{p}}_t)) \quad (13)$$

Taking this factor l_m into (11), the term $\mathbb{I}\{o_{m,3} \le v_m\}$ can be reformulated as $\mathbb{I}\{\hat{v}_m(\tilde{\mathbf{p}}) \le v_m\}$, where

$$\hat{v}_m(\tilde{\mathbf{p}}) = \frac{(p_{t,3} - p_{r,3})d(\bar{\mathbf{c}}_m, \bar{\mathbf{p}}_r)}{d(\bar{\mathbf{c}}_m, \bar{\mathbf{p}}_r) + d(\bar{\mathbf{c}}_m, \bar{\mathbf{p}}_t)} + p_{r,3}. \quad (14)$$

Noted that the term $\mathbb{I}\{\hat{v}_m(\tilde{\mathbf{p}}) \le v_m\}$ is decoupled from $\mathbf{l}_m$, as all parameters in (14) are given by the locations of the TX, RX and grid cell, which facilitates preprocessing of the height condition for v_m to accelerate both training and inference.

C. Orientation Condition for the Reflective Zone

We further determine the geometric boundaries for $\mathbf{l}_m$ to ensure that the intersection $\bar{\mathbf{o}}_m = (o_{m,1}, o_{m,2})$ satisfies the orientation conditions in (12).

Denote $\mathbf{l}_m = (\bar{\mathbf{l}}_m, \bar{l}_{m,3})$, where $\bar{\mathbf{l}}_m = (\bar{l}_{m,1}, \bar{l}_{m,2}) \in \mathbb{R}^2$ is the ground projected vector. Recall that the virtual obstacle is abstracted into a rectangular board, which is represented as a line segment passing through $\bar{\mathbf{c}}_m$ in a top view as shown in Fig. 3(d), and it is perpendicular to $\bar{\mathbf{l}}_m$. Denote $\bar{\mathbf{c}}_m'$ and $\bar{\mathbf{c}}_m''$ as the two endpoints of the rectangular board shown in Fig. 3(d), and therefore, the reflection point $\bar{\mathbf{o}}_m$ must locate in the line segment between the two endpoints $\bar{\mathbf{c}}_m'$ and $\bar{\mathbf{c}}_m''$. Define $\mathbf{b}_m'(\tilde{\mathbf{p}})$ as the normal vector of the virtual board when the reflection point locates at $\bar{\mathbf{c}}_m'$. It follows that

$$(\bar{\mathbf{c}}_m' - \bar{\mathbf{c}}_m) \cdot \mathbf{b}_m'(\tilde{\mathbf{p}}) = 0. \quad (15)$$

Then, according to the law of specular reflection, the incident angle $\angle(\mathbf{b}_m'(\tilde{\mathbf{p}}), \overrightarrow{\bar{\mathbf{c}}_m'\bar{\mathbf{p}}_r})$ equals to the emergence angle $\angle(\mathbf{b}_m'(\tilde{\mathbf{p}}), \overrightarrow{\bar{\mathbf{c}}_m'\bar{\mathbf{p}}_t})$, leading to the relation

$$\mathbf{b}_m'(\tilde{\mathbf{p}}) = (\bar{\mathbf{p}}_r - \bar{\mathbf{c}}_m')/ \|\bar{\mathbf{p}}_r - \bar{\mathbf{c}}_m'\| + (\bar{\mathbf{p}}_t - \bar{\mathbf{c}}_m')/ \|\bar{\mathbf{p}}_t - \bar{\mathbf{c}}_m'\|. \quad (16)$$

Similarly, define $\mathbf{b}_m''(\tilde{\mathbf{p}})$ as the normal vector of the virtual board when the point $\bar{\mathbf{o}}_m$ locates at $\bar{\mathbf{c}}_m''$. Intuitively, when the point $\bar{\mathbf{o}}_m$ locates on the line segment between $\bar{\mathbf{c}}_m'$ and $\bar{\mathbf{c}}_m''$, the normal vector $\bar{\mathbf{l}}_m$ lies in the convex hull of $\mathbf{b}_m'(\tilde{\mathbf{p}})$ and $\mathbf{b}_m''(\tilde{\mathbf{p}})$. This result is formally proven in the following lemma.

Lemma 1. *If there is a path $\tilde{\mathbf{p}}$ reflected by the mth obstacle, the vectors $\mathbf{b}_m'(\tilde{\mathbf{p}})$, $\mathbf{b}_m''(\tilde{\mathbf{p}})$ and the normal vector $\bar{\mathbf{l}}_m$ satisfy*

$$\angle(\mathbf{b}_m'(\tilde{\mathbf{p}}), \bar{\mathbf{l}}_m) + \angle(\mathbf{b}_m''(\tilde{\mathbf{p}}), \bar{\mathbf{l}}_m) = \angle(\mathbf{b}_m'(\tilde{\mathbf{p}}), \mathbf{b}_m''(\tilde{\mathbf{p}})) \quad (17)$$

where $\angle(\boldsymbol{x}, \boldsymbol{y}) = \arccos\left((\boldsymbol{x} \cdot \boldsymbol{y})/(\|\boldsymbol{x}\|\,\|\boldsymbol{y}\|)\right)$ represents the angle between the two vectors $\boldsymbol{x}$ and $\boldsymbol{y}$.

Proof. See Appendix A. □

By Lemma 1, the orientation conditions in (12) can be directly verified using the conclusion in (17), thereby bypassing the need for the calculation in (11). Meanwhile, as $\mathbf{b}_m'(\tilde{\mathbf{p}})$ and $\mathbf{b}_m''(\tilde{\mathbf{p}})$ are independent of the trainable variables v_m and $\bar{\mathbf{l}}_m$, they are constants that can be precomputed before training.

Using the auxiliary vectors $\widehat{v}_m(\tilde{\mathbf{p}})$, $\mathbf{b}_m'(\tilde{\mathbf{p}})$ and $\mathbf{b}_m''(\tilde{\mathbf{p}})$, we now can derive a simplified expression for characterizing the reflective zone (12) as follows.

Proposition 1. *Equation (12) can be simplified to*

$$\mathbb{I}\{\mathbf{p}_r \in \tilde{\mathcal{Q}}_m(\mathbf{p}_t, \mathbf{V})\} = \mathbb{I}\{\bar{\mathbf{l}}_m \cdot \widehat{\mathbf{b}}_m(\tilde{\mathbf{p}}) \geq \mathbf{b}_m'(\tilde{\mathbf{p}}) \cdot \widehat{\mathbf{b}}_m(\tilde{\mathbf{p}})\}$$
$$\times \mathbb{I}\{v_m \geq \widehat{v}_m(\tilde{\mathbf{p}})\} \quad (18)$$

where $\widehat{\mathbf{b}}_m(\tilde{\mathbf{p}}) = (\mathbf{b}_m'(\tilde{\mathbf{p}})/\|\mathbf{b}_m'(\tilde{\mathbf{p}})\| + \mathbf{b}_m''(\tilde{\mathbf{p}})/\|\mathbf{b}_m''(\tilde{\mathbf{p}})\|)/2$ denotes the bisector vector of $\mathbf{b}_m'(\tilde{\mathbf{p}})$ and $\mathbf{b}_m''(\tilde{\mathbf{p}})$.

Proof. See Appendix B. □

It is observed that Proposition 1 has substantially simplified the expression of the reflective zone. First, the computation of $\mathbf{o}_m$ in (11) is not required and the number of indicator functions has been reduced, which helps reduce the risk of gradient vanishing or explosion. Second, the parameters v_m and $\mathbf{l}_m$ are separated in the two terms in (18), and thus, the coupling has been reduced. Third, the condition parameters $\mathbf{b}_m'(\tilde{\mathbf{p}})$, $\widehat{\mathbf{b}}_m(\tilde{\mathbf{p}})$ and $\widehat{v}_m(\tilde{\mathbf{p}})$ in (18) are all known for the link $\tilde{\mathbf{p}}$ and can be precomputed to accelerate training.

IV. NETWORK ARCHITECTURE AND TRAINING

In this section, we develop a neural network architecture tailored to the proposed propagation components for joint environmental geometry and MIMO beam map construction. Specifically, we transform the blockage relation (6) and reflective zone formulation (18) into neural network representations, enabling efficient feature propagation and gradient flow for training. Specialized network structures incorporating dense connection, layer reuse, and modular sub-networks would be explored to learn distinct propagation characteristics, which explicitly leverage the geometric priors embedded in the physical modeling process. The proposed physics-informed neural network architecture is shown in Fig. 4.

A. Overall Architecture

As illustrated in Fig. 4, the proposed network consists of two main modules, *Area Activation* and *Channel Prediction*. The Area Activation module is designed to identify the relevant local virtual obstacles for the link $\tilde{\mathbf{p}}$ corresponding to each propagation component, while the Channel Prediction module models their interactions for accurate channel prediction.

1) Area Activation: This module selects a subset of virtual obstacles relevant to the link $\tilde{\mathbf{p}}$ and the beamforming vector $\mathbf{w}_j$. As a result, only the subset of the selected virtual obstacles are activated. For this purpose, four distinct area filters are defined, each structured as an $M_1 \times M_2$ matrix, matching the size of the virtual environment.

For the blockage component, a 3D line structure $\mathbf{Z}$ is constructed, where we project the altitude of the direct line connecting $\mathbf{p}_t$ and $\mathbf{p}_r$ to the ground. Thus, the mth element of the matrix $\mathbf{Z}$ is given by $Z_m = (p_{t,3} - p_{r,3})\frac{\|\bar{\mathbf{c}}_m - \bar{\mathbf{p}}_r\|}{\|\bar{\mathbf{p}}_t - \bar{\mathbf{p}}_r\|} + p_{r,3}$, if $m \in \mathcal{B}(\tilde{\mathbf{p}})$; and $Z_m = 0$, for $m \notin \mathcal{B}(\tilde{\mathbf{p}})$. The feature map of Area Activation for the blockage component is obtained by

$$\mathbf{O}_Z = \text{ReLU}((\mathbf{V}_H - \mathbf{Z}) \odot \mathbf{Z}) \quad (19)$$

where $\text{ReLU}(x) = \max(x, 0)$ and $\odot$ is the Hadamard product. The non-zero elements of $\mathbf{O}_Z$ indicate the locations where the propagation is blocked along the direct path.

For the reflection component, a main lobe mask $\mathbf{M}$ and a height matrix $\mathbf{R}$ are defined. In the main lobe mask $\mathbf{M}$, each entry M_m takes value 1 if $|\varphi(\mathbf{p}_t, \mathbf{c}_m) - \theta_j| \leq \Theta_j/2$; otherwise it takes a value 0. In the height matrix $\mathbf{R}$, the mth entry denotes the height condition $\widehat{v}_m(\tilde{\mathbf{p}})$ from (14) at the mth grid cell for the link $\tilde{\mathbf{p}}$. Thus, the feature map of Area Activation for the reflection component is given by

$$\mathbf{O}_R = \text{sign}(\text{ReLU}(\mathbf{V}_H - \mathbf{R})) \odot \mathbf{M} \quad (20)$$

where $\text{sign}(x) = \mathbb{I}\{x > 0\}$. The non-zero elements of $\mathbf{O}_R$ indicate the potential reflection locations within the main lobe.

For the scattering component, an ellipse mask $\mathbf{E}$ is constructed to select local obstacles for a link $\tilde{\mathbf{p}}$. Each entry E_m takes value 1 if $m \in \mathcal{B}_s(\tilde{\mathbf{p}}, \mathbf{V})$, and 0 otherwise. The feature map of Area Activation for the scattering is given by

$$\mathbf{O}_S = \mathbf{V}_H \odot \mathbf{E} \quad (21)$$

where the non-zero elements of $\mathbf{O}_S$ correspond to the local geometric features of the selected obstacles.

2) Channel Prediction: It includes four branches. The first branch takes the feature map $\mathbf{O}_Z$ to predict the path loss of the direct path. The second branch learns the beam pattern. The third branch takes the feature map $\mathbf{O}_R$ to form the reflective zone and estimate the reflected paths within it. The final branch takes the feature map $\mathbf{O}_S$ to capture the residual fluctuation due to scattering. The details are illustrated as follows.

B. The Beam Pattern Gain

The beam pattern $B(\cdot)$ is learned using a fully connected dense neural network (FC-DsNet). As illustrated in Fig. 4, the architecture comprises a feedforward layer, followed by a stack of three identical dense blocks, and concludes with
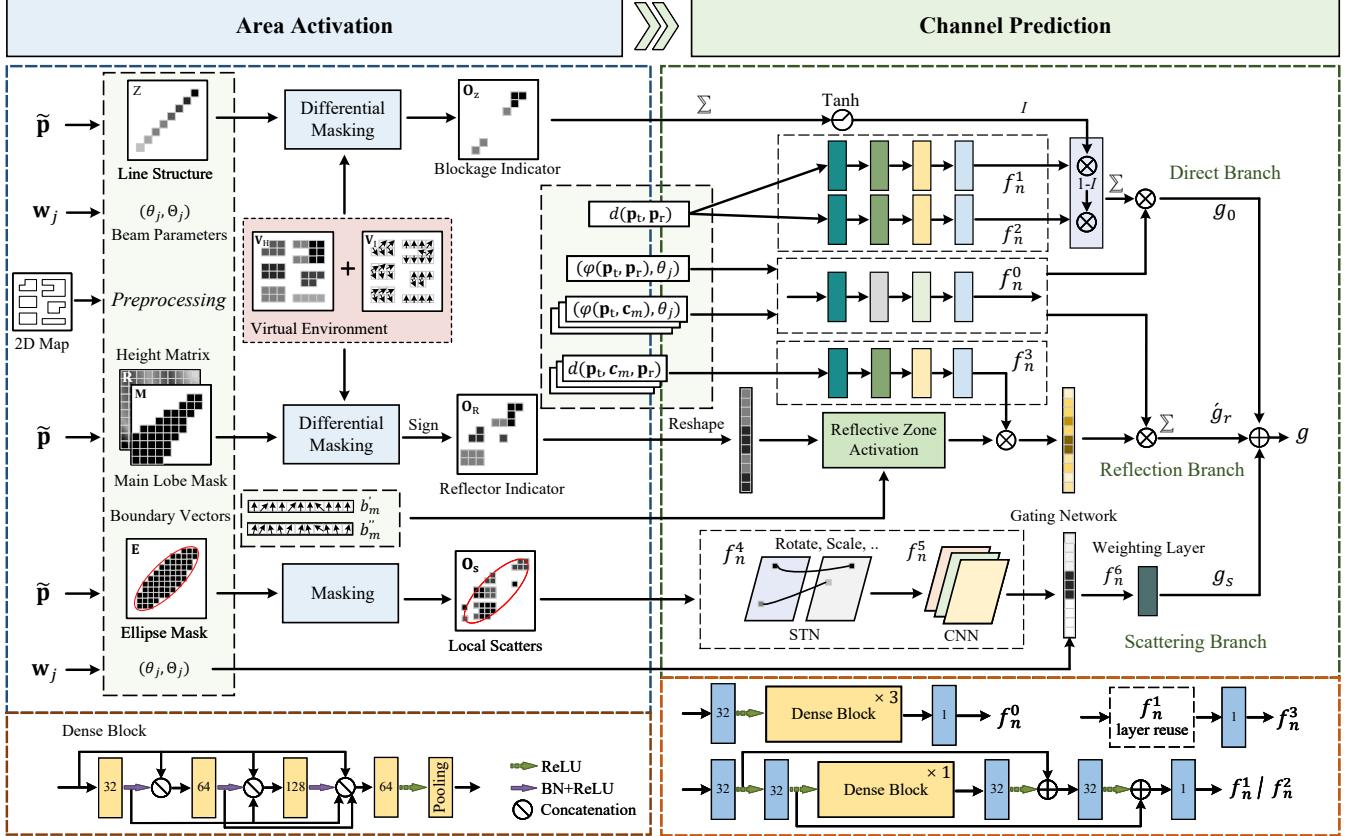
Figure 4. The physics-informed neural network architecture for joint MIMO beam map and virtual environment reconstruction.

a final feedforward layer. Each dense block contains three feedforward layers, with a batch normalization (BN) layer and a ReLU layer between them. Through dense connections, each layer receives and concatenates feature maps from all preceding layers, and then forwards them to the next layer, which facilitates direct gradient flow between layers, mitigating the vanishing gradient problem and enhancing information flow throughout the network. Finally, a feedforward layer merges the features, followed by a pooling layer that halves the feature dimensions. For an arbitrary location x relative to $\mathbf{p}_t$, the beam pattern component is implemented by

$$B(\varphi(\mathbf{p}_t, x), \mathbf{w}_j) = f_n^0([\varphi(\mathbf{p}_t, x); \theta_j]) \qquad (22)$$

where $f_n^0(\cdot)$ represents the mapping of the proposed FC-DsNet, and $[\varphi(\mathbf{p}_t, x); \theta_j]$ denotes the concatenation of the azimuth angle $\varphi(\mathbf{p}_t, x)$ and the beam angle θ_j.

C. The Blockage-Aware Direct Branch

The blockage branch is designed to implement the blockage relation (6) to characterize LOS and NLOS conditions, which is approximated by a tanh function to ensure a non-degenerated gradient for training. The design of the soft indicator function for the LOS region $\tilde{\mathcal{D}}_0(\mathbf{V}_H)$ is given as

$$I = 1 - \tanh(\text{sum}(\mathbf{O}_Z)\sigma_0) \qquad (23)$$

where $\text{sum}(\mathbf{A}) = \sum_{ij} a_{ij}$, $\tanh(x) = (e^x - e^{-x})/(e^x + e^{-x})$, and σ_0 is a scalar parameter. Consequently, when the feature

map $\mathbf{O}_Z$ contains all zeros, the direct path is not blocked by any virtual obstacle, we have the indicator $I = 1$. With the indicator I, the blockage-aware channel model of the direct path in (7) is implemented using two parallel FC-DsNets as

$$g_0(\tilde{\mathbf{p}}, \mathbf{V}_H) = I f_n^1(d(\mathbf{p}_t, \mathbf{p}_r)) + (1 - I) f_n^2(d(\mathbf{p}_t, \mathbf{p}_r)) \qquad (24)$$

where $f_n^1(\cdot)$ and $f_n^2(\cdot)$ denote the two parallel FC-DsNets. The networks $f_n^1(\cdot)$ and $f_n^2(\cdot)$ share the same architecture but differ from $f_n^0(\cdot)$ as they serve distinct tasks. As illustrated in Fig. 4, the network architecture includes two feedforward layers, followed by a dense block, and ends with three feedforward layers. The feedforward layers at both ends of the dense block are connected via skip connections. This structure can help reduce network complexity compared to fully dense connections while still preserving effective gradient propagation.

D. The Reflection Branch

The reflection branch is designed to aggregate reflected paths within the reflective zones. Define $\mathbf{B}', \widehat{\mathbf{B}} \in \mathbb{R}^{M_1 M_2 \times 2}$ as the matrix representations of all $\mathbf{b}'_m(\tilde{\mathbf{p}})$ and $\widehat{\mathbf{b}}_m(\tilde{\mathbf{p}})$ for the link $\tilde{\mathbf{p}}$, respectively. For operation alignment, a similar notation $\mathbf{V}_I \in \mathbb{R}^{M_1 M_2 \times 2}$ is also constructed for the normal vector $\bar{\mathbf{l}}_m$ for all grid cells. The neural network representation of the reflective zone in (18) is thus implemented by

$$\mathbf{r} = \tanh(\text{ReLU}(F(\mathbf{B}', \widehat{\mathbf{B}}, \mathbf{V}_I))\overline{\mathbf{O}_R}\sigma_1) \qquad (25)$$

and

$$F(\mathbf{B}', \widehat{\mathbf{B}}, \mathbf{V}_\mathrm{I}) = \mathrm{sumc}(\mathbf{V}_\mathrm{I} \odot \widehat{\mathbf{B}}) - \mathrm{sumc}(\mathbf{B}' \odot \widehat{\mathbf{B}}) \quad (26)$$

where $\overline{\mathbf{O}_\mathrm{R}} = \mathrm{vec}(\mathbf{O}_\mathrm{R})$ denotes the column vectorization of a matrix, σ_1 is a scalar parameter, and $\mathrm{sumc}(\cdot)$ represents the row-wise summation operation. For the impact of blockage, define $\varGamma_m$ as the LOS indicator that takes value 1 if neither the link $(\mathbf{p}_\mathrm{t}, \mathbf{c}_m)$ nor $(\mathbf{c}_m, \mathbf{p}_\mathrm{r})$ is blocked by any virtual obstacle, as the implementation in (23). As a result, the reflection via the mth oriented virtual obstacle in (9) is obtained by

$$g_\mathrm{r}^m(\tilde{\mathbf{p}}, \mathbf{w}_j, \mathbf{V}) = r_m \varGamma_m f_n^3(d'(\tilde{\mathbf{p}}, \mathbf{c}_m)) + (1 - r_m \varGamma_m)\tau \quad (27)$$

where r_m denotes the mth element of vector $\mathbf{r}$, $f_n^3(\cdot)$ is the neural network, and τ specifies the minimum cutoff threshold for gain. The network $f_n^3(\cdot)$ reuses all network layers of $f_n^1(\cdot)$ and adds a feedforward layer to predict the final path gain. This design implies that the signal attenuation of reflected paths and direct paths in free space share some similar characteristics.

E. The Scattering Branch

The scattering branch is designed to capture the spatial invariance property of the model (10) and to map the local environment to residual scattering. We adopt the neural network from [25], which integrates a spatial transformation network (STN) to capture rotation and scaling invariance, and a CNN to extract structural similarities from the local geometry of $\mathbf{V}$ for scattering mapping. Note that the design in [25] does not account for beam characteristics or support beam selection. To address this limitation, we extend its output to incorporate beam expansion and design a gating network to achieve beam selectivity. Thus, the scattering implementation is given by

$$g_\mathrm{s}(\tilde{\mathbf{p}}, \mathbf{w}_j, \mathbf{V}) = f_n^6(f_n^5(f_n^4(\mathbf{O}_\mathrm{S}))H(\mathbf{w}_j)) \quad (28)$$

where $f_n^4(\cdot)$, $f_n^5(\cdot)$ denote the STN and CNN, respectively, $H(\mathbf{w}_j)$ is a gating network that selects the contributing beams, and $f_n^6(\cdot)$ is a weighting layer for the selected beams.

Specifically, we extend the output dimension of the CNN to $|\mathcal{W}|$, each corresponding to a specific beam in the codebook. The gating network $H(\mathbf{w}_j)$ then produces a multi-hot output that selects index j and its neighbors, while setting all other entries to zero. The final weighting layer $f_n^6(\cdot)$ learns to assign weights to the selected beams through training.

F. Neural Network Training

We implement the proposed network using the deep learning library Pytorch and train it in a supervised manner using the Adam optimizer. Moreover, we employ a hybrid learning algorithm that combines particle swarm optimization (PSO) with Adam algorithm to update the parameter $\mathbf{V}_\mathrm{I}$. In each iteration, PSO introduces perturbations to the current solution for a broader global exploration, followed by Adam algorithm for local fine-tuning. This hybrid strategy combines the global exploration capability of PSO to escape local optima and the fine-tuning efficiency of Adam algorithm for convergence.

V. SIMULATIONS

The experiments are conducted using simulated channel data generated by a RT software, *Remcom Wireless Insite*.

In the simulation, the region of interest is a 640 m $\times$ 640 m square area with 9 TXs mounted at a height of 50 m. Each TX is equipped with a 16-element MIMO antenna array, and the DFT codebook is used. Ground RXs are fixed at a height of 2 m. Several buildings are included to enhance channel diversity. Channel data are generated with up to 6 reflections and 1 diffraction. A sinusoidal waveform at 2.8 GHz with 100 MHz bandwidth is used. In total, over 120 beam maps are generated, comprising more than 500,000 channel samples that capture rich propagation characteristics, including blockage and reflection, thereby providing a comprehensive dataset for modeling and analysis.

The proposed model is compared with the following baselines, RadioUNet [12], RME-GAN [18], DeepCom [19], SVT [26], and KNN, which are summarized as follows:

1) RadioUNet: This network consists of two UNets. The first takes the city map, sparse observations, and TX position as inputs to produce a coarse beam map, which is then refined by the second UNet using both the coarse map and original inputs to generate the final beam map.
2) RME-GAN: This network utilizes UNet as the generator, which takes the city map, sparse observations and TX position as inputs for beam map generation.
3) DeepCom: This network employs a CNN-based encoder-decoder architecture that compresses the sparse observation map into a low-dimensional latent representation and then reconstructs the complete beam map from it.
4) SVT: The algorithm recovers a matrix by minimizing its nuclear norm, iteratively applying singular value decomposition and soft-thresholding to converge towards the original low-rank matrix.
5) KNN: The algorithm selects 6 measurement samples that are closest to $\tilde{\mathbf{p}}$ and forms the neighbor set $\mathcal{N}(\tilde{\mathbf{p}})$. The channel gain at $\tilde{\mathbf{p}}$ is given by $g(\tilde{\mathbf{p}}) = \mu^{-1} \sum_{i \in \mathcal{N}(\tilde{\mathbf{p}})} \omega(\tilde{\mathbf{p}}, \tilde{\mathbf{p}}^{(i)}) y^{(i)}$, where $\omega(\tilde{\mathbf{p}}, \tilde{\mathbf{p}}^{(i)}) = \exp[-\kappa || \tilde{\mathbf{p}} - \tilde{\mathbf{p}}^{(i)} ||_2^2]$ and $\mu = \sum_{i \in \mathcal{N}(\tilde{\mathbf{p}})} \omega(\tilde{\mathbf{p}}, \tilde{\mathbf{p}}^{(i)})$.

Specifically, data from 5 TXs, with nearly 30% of measurement samples from each unless otherwise specified, is used for training, while the remaining 4 TXs are reserved for testing. Since our focus is on high-energy regions, such as the main lobe of the beam, we truncate channel gains below a cutoff threshold for performance evaluation. The truncation function is defined as $\zeta(x) = \max(x, \eta)$, where η is a cutoff threshold, and it is set to -130 dB for all experiments. The mean absolute error (MAE) and the root mean square error (RMSE) between the truncated simulated gain $\zeta(y^{(i)})$ and the estimated gain $\zeta(g(\tilde{\mathbf{p}}^{(i)}, \mathbf{w}_j; \boldsymbol{\Theta}, \mathbf{V}))$ will serve as performance metrics. This approach aligns with practical cases where beamforming is designed to ensure high communication quality within a target region, while performance outside it is less critical.

A. Performance of the Proposed Reflection Component

In this experiment, we evaluate the improvement in MIMO beam map construction with the reflection component.
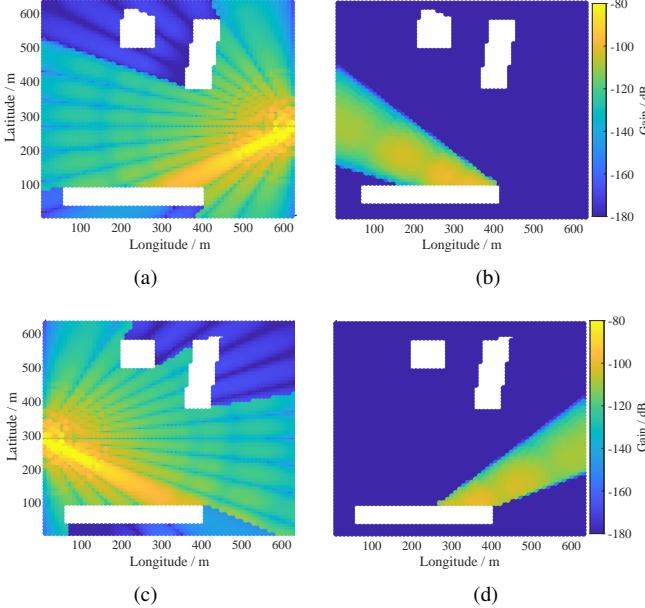
Figure 5. The direct and reflected beams are separated: a) and c) The beams from two TXs are blocked; b) and d) The corresponding reflected beams.

Table I
COMPARISON OF MIMO BEAM MAP WITH DIFFERENT DESIGN BRANCHES

Scheme	MAE / dB	RMSE / dB
Direct branch	3.144	5.737
Only direct + reflection	**2.491**	**4.461**
Direct + reflection + scattering	**2.016**	**3.941**

Table I presents a comparison of the MIMO beam map accuracy achieved by the proposed model with different design components involving blockage, reflection and scattering. The results show that incorporating both direct and reflected paths significantly improves performance compared to using only the direct branch, which results in a 20.7% reduction in MAE and a 22.4% reduction in RMSE. In addition, further extending the model to account for scattering leads to additional performance gains, with MAE and RMSE further reduced by 19.1% and 11.6%, respectively, thereby demonstrating the effectiveness of the proposed physics-informed components.

Fig. 5 illustrates the direct and reflected beams generated by the proposed model. The results show that the proposed model can reconstruct the radio beam geometry, including beam shape, direction, blockage, and reflection. For a specific obstacle, the proposed model can capture direct beams impinging on the obstacle from different TXs and directions, along with their corresponding reflected beams. As a result, the blockage and reflection components of a beam can be separated from only RSS measurements. This capability to identify blockage and reflection provides practical advantages in real-world applications, as further discussed in this paper.

B. Geometry of the Virtual Environment

We further illustrate the geometry of the environment captured by $\mathbf{V}$. Specifically, we assume the obstacle locations are
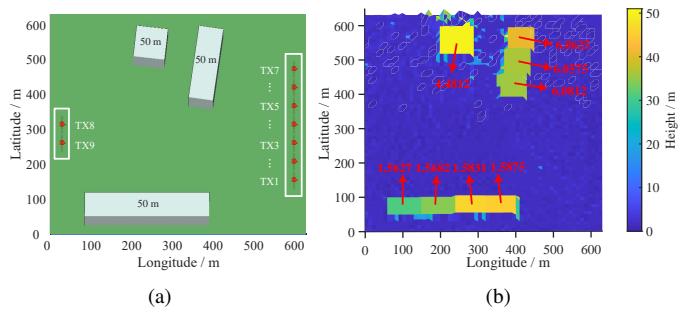

Figure 6. a) The 3D terrain of the simulated environment, where odd-numbered TXs (e.g., 1, 3, 5) are used for training and even-numbered TXs (e.g., 2, 4, 6) are used for testing; b) The oriented virtual obstacle map learned by the proposed model.

Table II
COMPARISON OF BEAM MAP ACCURACY WITH DIFFERENT METHODS.

Scheme	MAE / dB	RMSE / dB
RadioUNet [12]	3.171	5.763
RME-GAN [18]	3.889	6.499
DeepCom [19]	2.975	5.235
SVT [26]	4.804	8.647
KNN	3.360	5.892
Proposed	**2.016**	**3.941**

known from a 2D map, which lacks height and orientation information. Each obstacle is further divided into smaller parts, with each part potentially spanning multiple grid cells, allowing each part to independently learn its own parameters.

Fig. 6(a) shows the 3D terrain of the simulated environment along with the deployment of the TXs, while the corresponding oriented virtual obstacle map, incorporating both the height information $\mathbf{V}_H$ and angle information $\mathbf{V}_\Phi$ is shown in Fig. 6(b). The results indicate that the geometry and distribution of the obstacles learned by the proposed model closely align with the simulated environment, demonstrating its ability to capture environmental geometry from RSS measurements.

Note that city maps usually do not correspond to the desired virtual environment maps, as they typically lack critical radio information such as electromagnetic coefficients. In Fig. 6(b), the height $\mathbf{V}_H$ does not have to exactly match the actual obstacle heights; instead, it is optimized so that the channel model (5) fits the RSS measurements. Consequently, different parts of the same obstacle may be assigned different heights. The normal angles $\mathbf{V}_\Phi$ for each obstacle align with their orientations in the simulated environment, and they also remain largely consistent across different parts of the same obstacle.

C. Comparison to Other State-of-the-arts

We compare the performance of the MIMO beam map construction of the proposed model and the baselines.

Two slices of the MIMO beam maps are presented in Fig. 7, where Fig. 7(a) illustrates a reflection-involved scenario, and Fig. 7(b) shows a direct beam case without reflection. The results show that the proposed model clearly delineates the beam
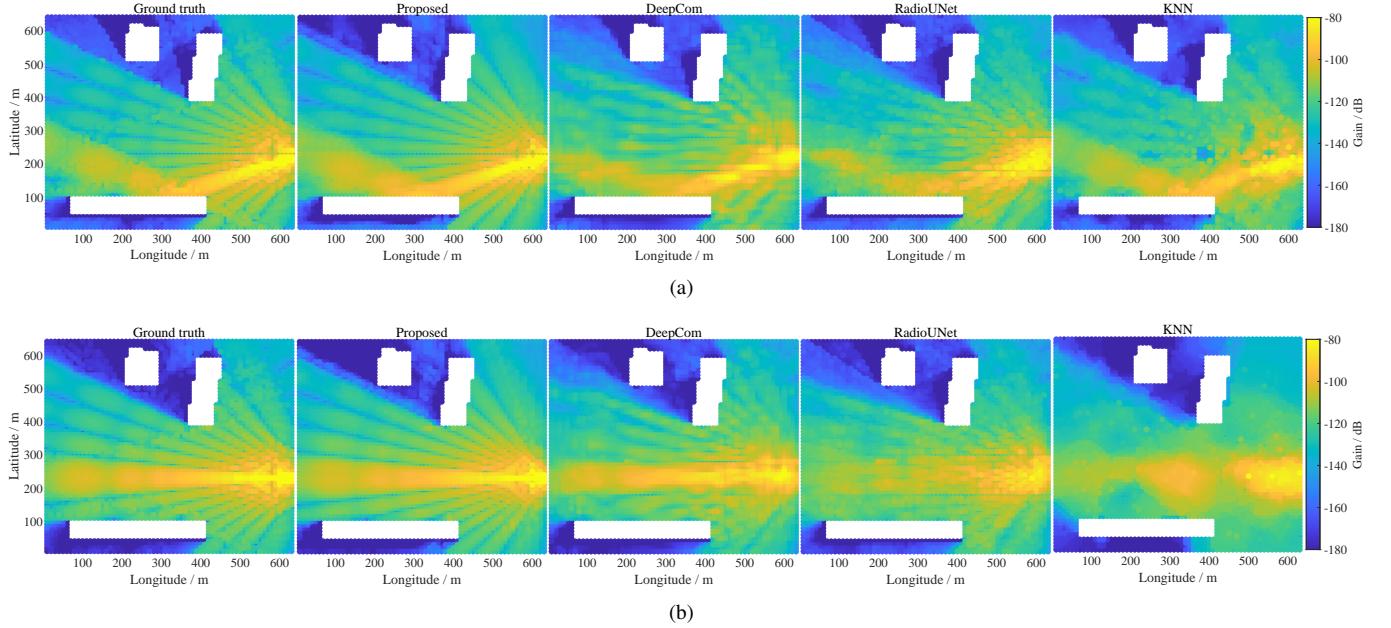
Figure 7. The ground truth and reconstructed MIMO beam maps: a) The reflected beam maps constructed under 30% training samples; b) The direct beam maps without reflections constructed under 5% training samples.
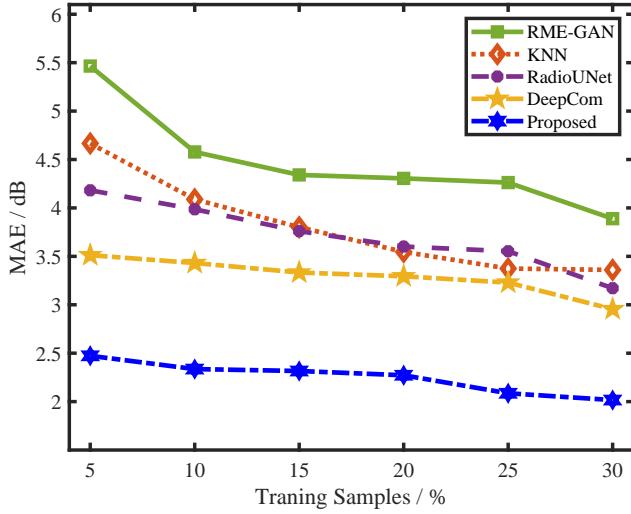

Figure 8. Reconstruction MAE versus the ratio of training samples.

in obstructed environments. In addition, unlike other baselines that require extra input measurements during inference, the proposed model does not require any additional data to operate after training, making it more practical for real-world deployment while maintaining superior accuracy.

In addition, we evaluate beam map construction across various training sample ratios, ranging from 5% to 30%. Fig. 8 illustrates the relationship between the MAE and the training samples. It is observed that RME-GAN, KNN, and RadioUNet suffer significant performance drops as the training samples decrease, whereas the proposed model and DeepCom degrade slightly. In contrast, the proposed model exhibited exceptional stability with merely a 0.4 dB variation in MAE, which shows strong robustness and data efficiency. Notably, the proposed model also outperforms all baselines in all cases, demonstrating our superiority in achieving high accuracy even with substantially reduced data requirements.

D. Performance of New Beam Extrapolation

In this section, we demonstrate that the proposed model can extrapolate new beams, with its capability to predict beams for previously unseen scenarios beyond the training data.

To this end, 10 beam maps of a specific TX are used for training, while the remaining maps are reserved for prediction. We consider two experimental cases: I) training and test beam maps are selected alternately (e.g., beams 1, 3, 5 for training and 2, 4, 6 for testing); II) the first 10 beam maps are directly used for training, and the rest for testing. As a result, in Case I, adjacent beams in the training and test sets may exhibit partial spatial overlap, while in Case II, such overlap occurs only for the first test beam. We further assume the environment is known, such that our model can capture reflection features from unknown obstacles and previously unseen beam directions, as these can be learned from other

direction and width, as well as both incident and reflected beams. By contrast, although the baselines can partially learn beam shapes and reflection with 30% of the training samples, only DeepCom performs well at 5%, as the others fail to capture beam features. This highlights the advantage of the proposed model in beam reconstruction across both scenarios.

Table II presents the MAE and RMSE of various methods for beam map construction. The proposed model significantly outperforms all baselines across both metrics. Compared to mainstream deep learning approaches, such as RadioUNet, RME-GAN, and DeepCom, it achieves an improvement of $32.2\% - 48.1\%$ in MAE and $24.7\% - 39.3\%$ in RMSE. Among the baselines, SVT performs the worst, likely due to the limited effectiveness of such matrix completion technique
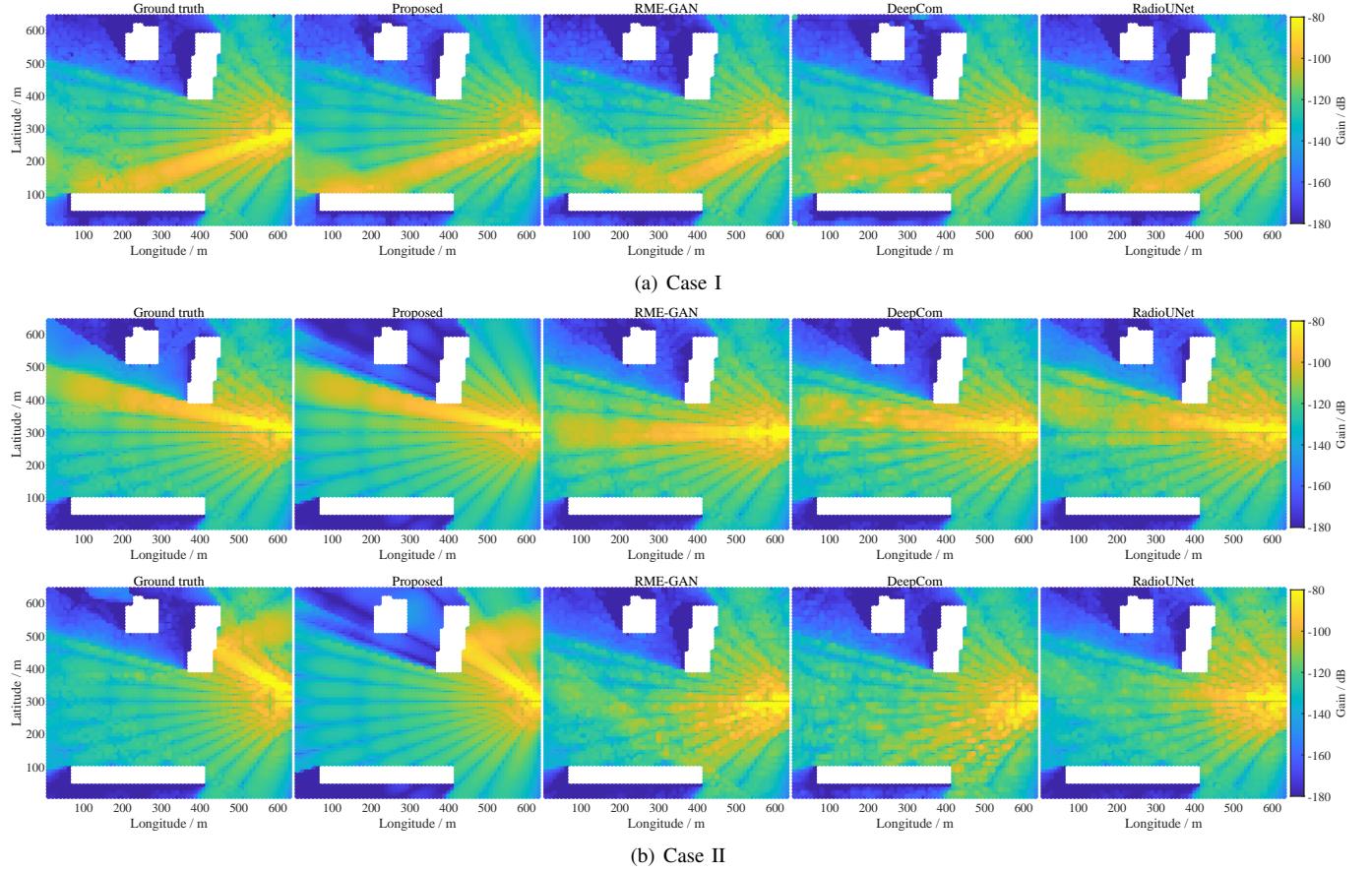
Figure 9. MIMO beam extrapolation: a) Trained on odd-numbered beams and tested on beam No. 6; b) Trained on beams 1-10, and tested on beam No. 11 and 14.

TXs. Note that in Case II, we omit the scattering branch from the proposed model and evaluate its extrapolation capability only for the direct and reflection branches.

The beam extrapolation results are shown in Fig. 9. In Case I, the proposed model can generate previously unseen beams, with the predictions closely matching the simulated ones, while the baselines perform poorly. Specifically, Deep-Com fails to generate clear beam patterns, and both RME-GAN and RadioUNet incorrectly predict the target beam as a different known beam, likely approximating the unseen beam by selecting the closest match from the training set. Similar outcomes are observed for the first extrapolated beam in Case II, as shown in the first row of Fig. 9(b). For the other beams, all baselines fail to extrapolate completely unseen beams with no spatial overlap, revealing their limited generalization beyond the training data. In contrast, the proposed model successfully extrapolates these beams, demonstrating superior extrapolation capability.

E. Transferability to a New Environment

We demonstrate the transferability of the proposed model to a new environment. The geometric parameters of the new environment will be input to initialize the virtual environment parameters **V**, thereby adapting the model to the new context.

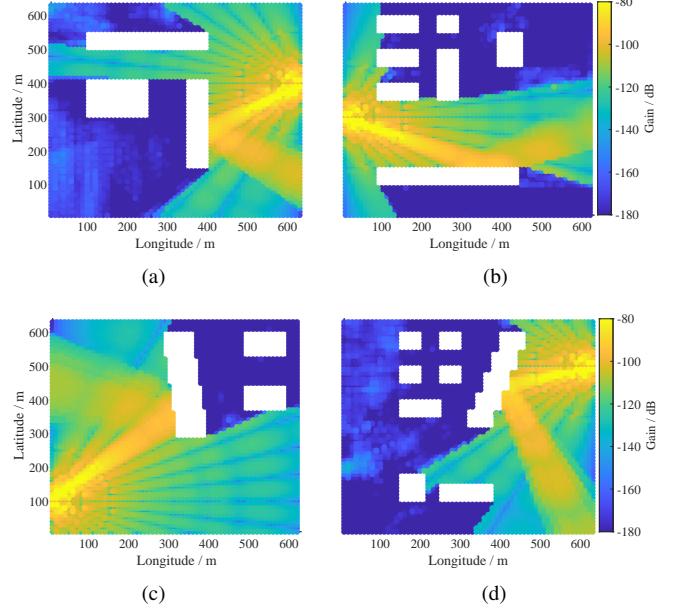Fig. 10 shows the beam maps generated by the proposed model across 4 distinct environments with varying TX posi-

Figure 10. MIMO beam maps generated by the proposed model transferred to a new environment with the knowledge of the oriented virtual obstacles **V**, where the trained propagation parameters are fixed.

tions and obstacle configurations. It is observed that the proposed model accurately predicts beam patterns in previously

unseen environments based on their geometric parameters, TX locations and beam angles. The relationship between incident beams, reflections, and obstacles remains consistent and predictable. Notably, the model generalizes well across varying TX positions, indicating that it learns relative spatial features rather than memorizing absolute locations. Consequently, as long as environment parameters are available or pre-estimated, the model can adapt to diverse scenarios without retraining, ensuring efficiency and scalability for deployment.

F. Application in Site-Specific Beam Alignment

This section discusses the advantages of recognizing blockage and reflection for online beam alignment.

We consider to select an optimal beamforming vector $\mathbf{w}_j$ from a predefined codebook $\mathcal{W}$ at the TX to align the beam toward a specific RX to maximize the communication quality. The beam alignment problem is to find the beam index that maximizes the signal-to-noise ratio (SNR):

$$j^* = \underset{j \in \{1,..,|\mathcal{W}|\}}{\operatorname{argmax}} \frac{|\mathbf{h}_d(\tilde{\mathbf{p}})\mathbf{w}_j|^2 P_s}{\sigma^2} \quad (29)$$

where P_s denotes the transmitted power and σ^2 is the noise power. Here $\mathbf{h}_d(\tilde{\mathbf{p}}) = \mathbf{h}(\tilde{\mathbf{p}}) + \mathbf{h}^\epsilon$ represents the dynamic channel, where $\mathbf{h}^\epsilon$ captures uncertainty due to environmental dynamics (e.g., moving scatterers). In this problem, beam sweeping is employed to identify the optimal beam index j^* from the codebook $\mathcal{W}$.

We propose an environment-aware beam sweeping strategy to reduce search overhead by leveraging learned environmental geometry. Specifically, the beam is steered towards the RX in LOS regions, and in NLOS regions, the search is guided by valid reflected paths, which are summarized as follows:

- If $\mathbb{I}\{\tilde{\mathbf{p}} \in \tilde{\mathcal{D}}_0(\mathbf{V}_H)\}$, then $j^* = \operatorname{argmin}_j |\varphi(\mathbf{p}_t, \mathbf{p}_r) - \theta_j|$ and no probing overhead is required.
- If $\mathbb{I}\{\tilde{\mathbf{p}} \in \tilde{\mathcal{D}}_1(\mathbf{V}_H)\}$, the beam directions are searched based on valid reflected paths that satisfy both $\varphi(\mathbf{p}_t, \mathbf{c}_m) \in [\theta_j \pm \Theta_j/2]$ and $\mathbb{I}\{\mathbf{p}_r \in \tilde{\mathcal{Q}}_m(\mathbf{p}_t, \mathbf{V})\}$, as verified by equation (25).
- If $\mathbb{I}\{\tilde{\mathbf{p}} \in \tilde{\mathcal{D}}_1(\mathbf{V}_H)\}$ and no valid reflection exists, all beam directions are searched.

The following benchmarks are considered: 1) Exhaustive search: the best beam is chosen by sweeping all candidates; 2) Hierarchical search [27]: it repeatedly splits the space into two partitions and refines beam selection from wide to narrow beams; 3) Probing based method [28]: it jointly learns a compact probing codebook with channel $\mathbf{h}$ and predict the beam index via a classifier. We evaluate the beam alignment performance under $P_s = 30$ dBm and 20 dBm, respectively, with the noise power σ^2 set to -110 dBm.

Table III summarizes the average SNR across 100 RXs and the number of probing steps required by each method. Here, the probing step refers to the number of beam directions explored during the alignment process. It is observed that our map assisted approach achieves an SNR comparable to that of the exhaustive search while reducing the number of probing steps by 78%. Compared to hierarchical search, it improves the SNR by 6 dB and requires only half the number

Table III
APPLICATION IN BEAM ALIGNMENT

Scheme	P_s = 30 dBm		P_s = 20 dBm	
	Steps	SNR (dB)	Steps	SNR (dB)
Exhaustive search	1600	**26.79**	1600	**15.26**
Hierarchical search	800	19.10	800	9.17
Probing based method	400	21.33	400	4.79
Map assisted (ours)	**352**	**25.60**	**352**	**14.93**

of probing steps. Although the probing based method reduces the probing steps and achieves higher SNR when $P_s = 30$ dBm, its performance deteriorates significantly when P_s is reduced to 20 dBm.

VI. CONCLUSION

This paper developed a physics-informed neural network to learn the geometric features of the virtual environment for environment-aware MIMO beam map construction. In contrast to many existing deep learning approaches that lack an explicit environment model, an oriented virtual obstacle model was proposed to capture the environmental geometry by modeling signal behaviors of blockage and reflection. To characterize reflective propagation, we formulated the concept of the reflective zone, derived its expression, and reformulated it for improved compatibility with deep learning representations. By integrating this reflective-zone-based geometry model, a deep neural network architecture was designed to jointly learn the blockage, reflection and scattering components, as well as the beam pattern. Design examples showed a great superiority of the proposed model with over 30% improvement in beam map accuracy, along with strong extrapolation to unseen beams and transferability to new environments.

APPENDIX A
PROOF OF LEMMA 1

Figure 11. The geometry of orientation conditions for the reflective zone.

The proof of Lemma 1 proceeds in two steps. First, we show that if line l does not lie in the plane spanned by l' and l'', the point $\bar{\mathbf{o}}_m$ falls outside the valid circular region of l, violating the law of reflection. Second, we prove that if $\bar{\mathbf{o}}_m$ lies on l within the circular region, the lemma holds.

Consider the case where $\bar{\mathbf{o}}_m$ lies to the left of the center $\bar{\mathbf{c}}_m$. As shown in Fig. 11(a), line l is formed by rotating

l' counterclockwise by an angle θ, placing it outside the region bounded by l' and l''. Let TX^m and TX'^m denote the virtual TXs associated with l and l', located at $\bar{\mathbf{p}}_\text{t}^m$ and $\bar{\mathbf{p}}_\text{t}'^m$, respectively. Geometrically, triangles $\triangle a\bar{\mathbf{p}}_\text{t}'^m\bar{\mathbf{c}}_m$ and $\triangle a\bar{\mathbf{p}}_\text{t}\bar{\mathbf{c}}_m$ are congruent, implying that $||\bar{\mathbf{p}}_\text{t}'^m - \bar{\mathbf{c}}_m|| = ||\bar{\mathbf{p}}_\text{t} - \bar{\mathbf{c}}_m||$. Hence, the TX, TX^m and TX'^m all lie on the same outer circle centered at $\bar{\mathbf{c}}_m$ with radius $||\bar{\mathbf{p}}_\text{t} - \bar{\mathbf{c}}_m||$. As line l rotates, the virtual TX traces a circular arc. In addition, from the similarity of $\triangle ab\bar{\mathbf{c}}_m$ and $\triangle eb\bar{\mathbf{p}}_\text{t}$, it follows that $\angle \bar{\mathbf{p}}_\text{t}'^m\bar{\mathbf{p}}_\text{t}\bar{\mathbf{p}}_\text{t}^m = \theta$. As θ increases, TX^m moves counterclockwise along the outer circle, and the angle φ between the paths $\overrightarrow{\bar{\mathbf{p}}_\text{t}^m\bar{\mathbf{p}}_\text{r}}$ and $\overrightarrow{\bar{\mathbf{p}}_\text{t}'^m\bar{\mathbf{p}}_\text{r}}$ also increases. Consequently, $\bar{\mathbf{o}}_m$ shifts further from $\bar{\mathbf{c}}_m$, leading to $||\bar{\mathbf{o}}_m - \bar{\mathbf{c}}_m|| \geq ||\bar{\mathbf{c}}_m' - \bar{\mathbf{c}}_m||$, which implies $\bar{\mathbf{o}}_m$ lies outside the grid cell, violating the orientation condition in (12). Thus, line l must lie within the shadow region spanned by l' and l''.

We further verify the conclusion by showing that when a reflected path exists, the line l lies within the region bounded by l' and l''. In Fig. 11(b), extend the vectors $\mathbf{b}_m'$ and $\mathbf{b}_m''$ from points $\bar{\mathbf{c}}_m'$ and $\bar{\mathbf{c}}_m''$ in the opposite direction to intersect line l at points $\boldsymbol{\alpha}_m'$ and $\boldsymbol{\alpha}_m''$, respectively. By the triangle angle sum property, we obtain $\angle(\mathbf{b}_m', \overrightarrow{\boldsymbol{\alpha}_m'\bar{\mathbf{c}}_m}) < \pi/2$ and $\angle(\mathbf{b}_m'', \overrightarrow{\bar{\mathbf{c}}_m\boldsymbol{\alpha}_m''}) > \pi/2$. Given $\angle(\bar{\mathbf{l}}_m, \overrightarrow{\bar{\mathbf{c}}_m\boldsymbol{\alpha}_m''}) = \pi/2$, it follows that $\angle(\mathbf{b}_m'', \overrightarrow{\bar{\mathbf{c}}_m\boldsymbol{\alpha}_m''}) - \angle(\mathbf{b}_m', \overrightarrow{\boldsymbol{\alpha}_m'\bar{\mathbf{c}}_m}) = \angle(\mathbf{b}_m'', \overrightarrow{\bar{\mathbf{c}}_m\boldsymbol{\alpha}_m''}) - \angle(\bar{\mathbf{l}}_m, \overrightarrow{\bar{\mathbf{c}}_m\boldsymbol{\alpha}_m''}) + \angle(\bar{\mathbf{l}}_m, \overrightarrow{\boldsymbol{\alpha}_m'\bar{\mathbf{c}}_m}) - \angle(\mathbf{b}_m', \overrightarrow{\boldsymbol{\alpha}_m'\bar{\mathbf{c}}_m})$, which yields the final result $\angle(\mathbf{b}_m', \mathbf{b}_m'') = \angle(\mathbf{b}_m', \bar{\mathbf{l}}_m) + \angle(\mathbf{b}_m'', \bar{\mathbf{l}}_m)$.

APPENDIX B
PROOF OF PROPOSITION 1

According to Lemma 1, the orientation conditions in the first two terms of (12) can be reformulated as $\prod_{i=\{1,2\}} \mathbb{I}\{|o_{m,i} - c_{m,i}| \leq D/2\} \mathbb{I}\{(\mathbf{l}_m \cdot (\mathbf{c}_m - \mathbf{p}_\text{r})) / (\mathbf{l}_m \cdot (\mathbf{p}_\text{t}^m - \mathbf{p}_\text{r}))\} = \mathbb{I}\{\angle(\mathbf{b}_m', \bar{\mathbf{l}}_m) + \angle(\mathbf{b}_m'', \bar{\mathbf{l}}_m) = \angle(\mathbf{b}_m', \mathbf{b}_m'')\}$. Here we omit $\tilde{\mathbf{p}}$ for simplicity. On the right-hand side, since both $\angle(\widehat{\mathbf{b}}_m, \mathbf{b}_m')$ and $\angle(\widehat{\mathbf{b}}_m, \bar{\mathbf{l}}_m)$ are acute, it follows that $\angle(\widehat{\mathbf{b}}_m, \bar{\mathbf{l}}_m) \leq \angle(\widehat{\mathbf{b}}_m, \mathbf{b}_m')$, and thus, $\cos\angle(\widehat{\mathbf{b}}_m, \mathbf{l}_m) \geq \cos\angle(\widehat{\mathbf{b}}_m, \mathbf{b}_m')$. This is equivalent to $\bar{\mathbf{l}}_m \cdot \widehat{\mathbf{b}}_m / (||\bar{\mathbf{l}}_m|| \, ||\widehat{\mathbf{b}}_m||) \geq \mathbf{b}_m' \cdot \widehat{\mathbf{b}}_m / (||\mathbf{b}_m'|| \, ||\widehat{\mathbf{b}}_m||)$. Since $\widehat{\mathbf{b}}_m$ and $\mathbf{b}_m'$ are known a priori, we normalize them to unit vectors, which confirms the first term. The second term follows directly from (14).

REFERENCES

[1] C. Wei, K. Xu, Z. Shen, X. Xia, C. Li, W. Xie, D. Zhang, and H. Liang, "Fingerprint-based localization and channel estimation integration for cell-free massive MIMO IoT systems," *IEEE Internet Things J.*, vol. 9, no. 24, pp. 25 237–25 252, 2022.

[2] W. Feng, Y. Lin, Y. Wang, J. Wang, Y. Chen, N. Ge, S. Jin, and H. Zhu, "Radio map-based cognitive satellite-UAV networks towards 6G on-demand coverage," *IEEE Trans. Cognit. Commun. Networking*, vol. 10, no. 3, pp. 1075–1089, 2024.

[3] W. B. Chikha, M. Masson, Z. Altman, and S. B. Jemaa, "Radio environment map based inter-cell interference coordination for massive-MIMO systems," *IEEE Trans. Mob. Comput.*, vol. 23, no. 1, pp. 785–796, 2024.

[4] Q. Xue, C. Ji, S. Ma, J. Guo, Y. Xu, Q. Chen, and W. Zhang, "A survey of beam management for mmwave and THz communications towards 6G," *IEEE Commun. Surv. Tutor.*, vol. 26, no. 3, pp. 1520–1559, 2024.

[5] Y. Hu and R. Zhang, "A spatiotemporal approach for secure crowd-sourced radio environment map construction," *IEEE/ACM Trans. Netw.*, vol. 28, no. 4, pp. 1790–1803, 2020.

[6] N. Dal Fabbro, M. Rossi, G. Pillonetto, L. Schenato, and G. Piro, "Model-free radio map estimation in massive MIMO systems via semi-parametric gaussian regression," *IEEE Wireless Commun. Lett.*, vol. 11, no. 3, pp. 473–477, 2022.

[7] C. Phillips, M. Ton, D. Sicker, and D. Grunwald, "Practical radio environment mapping with geostatistics," in *Proc. IEEE Int. Symp. Dyn. Spectr. Access Netw.*, 2012, pp. 422–433.

[8] Y. Zhang and S. Wang, "K-Nearest neighbors Gaussian process regression for urban radio map reconstruction," *IEEE Commun. Lett.*, vol. 26, no. 12, pp. 3049–3053, 2022.

[9] H. Sun and J. Chen, "Integrated interpolation and block-term tensor decomposition for spectrum map construction," *IEEE Trans. Signal Process.*, vol. 72, pp. 3896–3911, 2024.

[10] G. Zhang, X. Fu, J. Wang, X.-L. Zhao, and M. Hong, "Spectrum cartography via coupled block-term tensor decomposition," *IEEE Trans. Signal Process.*, vol. 68, pp. 3660–3675, 2020.

[11] K. Saito, Y. Jin, C. Kang, J. ichi Takada, and J.-S. Leu, "Two-step path loss prediction by artificial neural network for wireless service area planning," *IEICE Commun. Exp.*, vol. 8, no. 12, pp. 611–616, 2019.

[12] R. Levie, Ç. Yapar, G. Kutyniok, and G. Caire, "RadioUNet: Fast radio map estimation with convolutional neural networks," *IEEE Trans. on Wireless Commun.*, vol. 20, no. 6, pp. 4001–4015, 2021.

[13] L. Wu, D. He, B. Ai, J. Wang, H. Qi, K. Guan, and Z. Zhong, "Artificial neural network based path loss prediction for wireless communication network," *IEEE Access*, vol. 8, pp. 199 523–199 538, 2020.

[14] D. He, B. Ai, K. Guan, L. Wang, Z. Zhong, and T. KÃŒrner, "The design and applications of high-performance ray-tracing simulation platform for 5G and beyond wireless communications: A tutorial," *IEEE Commun. Surv. Tutor.*, vol. 21, no. 1, pp. 10–27, 2019.

[15] M. Matalatala Tamasala, S. Shikhantsov, M. Deruyck, E. Tanghe, D. Plets, S. K. Goudos, L. Martens, and W. Joseph, "Combined ray-tracing/fdtd and network planner methods for the design of massive mimo networks," *IEEE Access*, vol. 8, pp. 206 371–206 387, 2020.

[16] L. Azpilicueta, M. Rawat, K. Rawat, F. M. Ghannouchi, and F. Falcone, "A ray launching-neural network approach for radio wave propagation analysis in complex indoor environments," *IEEE Trans. Antennas Propag.*, vol. 62, no. 5, pp. 2777–2786, 2014.

[17] V. V. Ratnam, H. Chen, S. Pawar, B. Zhang, C. J. Zhang, Y.-J. Kim, S. Lee, M. Cho, and S.-R. Yoon, "Fadenet: Deep learning-based mm-wave large-scale channel fading prediction and its applications," *IEEE Access*, vol. 9, pp. 3278–3290, 2021.

[18] S. Zhang, A. Wijesinghe, and Z. Ding, "RME-GAN: A learning framework for radio map estimation based on conditional generative adversarial network," *IEEE Internet Things J.*, vol. 10, no. 20, pp. 18 016–18 027, 2023.

[19] Y. Teganya and D. Romero, "Deep completion autoencoders for radio map estimation," *IEEE Trans. Wireless Commun.*, vol. 21, no. 3, pp. 1710–1724, 2022.

[20] P. Kazemi, H. Al-Tous, T. Ponnada, C. Studer, and O. Tirkkonen, "Beam SNR prediction using channel charting," *IEEE Trans. Veh. Technol.*, vol. 72, no. 10, pp. 13 130–13 145, 2023.

[21] J. Deng, O. Tirkkonen, J. Zhang, X. Jiao, and C. Studer, "Network-side localization via semi-supervised multi-point channel charting," in *in Proc. Int. Wireless Commun. Mob. Comput.*, 2021, pp. 1654–1660.

[22] C. Studer, S. Medjkouh, E. Gonultas, T. Goldstein, and O. Tirkkonen, "Channel charting: Locating users within the radio environment using channel state information," *IEEE Access*, vol. 6, pp. 47 682–47 698, 2018.

[23] B. R. Hamilton, X. Ma, R. J. Baxley, and S. M. Matechik, "Propagation modeling for radio frequency tomography in wireless networks," *IEEE J. Sel. Top. Signal Process.*, vol. 8, no. 1, pp. 55–65, 2014.

[24] W. Liu and J. Chen, "UAV-aided radio map construction exploiting environment semantics," *IEEE Trans. Wireless Commun.*, vol. 22, no. 9, pp. 6341–6355, 2023.

[25] W. Chen and J. Chen, "Diffraction and scattering aware radio map and environment reconstruction using geometry model-assisted deep learning," *IEEE Trans. Wireless Commun.*, vol. 23, no. 12, pp. 19 804–19 819, 2024.

[26] J. Cai, E. J. Candès, and Z. Shen, "A singular value thresholding algorithm for matrix completion," *SIAM J. Optim.*, vol. 20, no. 4, pp. 1956–1982, 2010.

[27] Z. Xiao, T. He, P. Xia, and X.-G. Xia, "Hierarchical codebook design for beamforming training in millimeter-wave communication," *IEEE Trans. Wireless Commun.*, vol. 15, no. 5, pp. 3380–3392, 2016.

[28] Y. Heng, J. Mo, and J. G. Andrews, "Learning site-specific probing beams for fast mmwave beam alignment," *IEEE Trans. Wireless Commun.*, vol. 21, no. 8, pp. 5785–5800, 2022.